Heliyon 10 (2024) e27439

Contents lists available at ScienceDirect

Heliyon

journal homepage: www.cell.com/heliyon

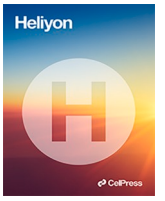

Research article

Experimental kinetics and thermodynamics investigation: Chemically activated carbon-enriched monolithic reduced graphene oxide for efficient CO_2 capture

Ranjeet Kumar Jha [a], Haripada Bhunia [b,**], Soumen Basu [a,*]

[a] Department of Chemistry and Biochemistry, Thapar Institute of Engineering and Technology, Patiala-147004, Punjab, India
[b] Department of Chemical Engineering, Thapar Institute of Engineering and Technology, Patiala-147004, Punjab, India

ARTICLE INFO

Keywords:
Monolith
Graphene-oxide
Chemically activated
CO_2 capture
Kinetic study
Thermodynamic study

ABSTRACT

In this research, we have developed solid MGOs by self-assembled reduction process of GO at 90 °C with different weight ratios of oxalic acid (1:1, 1:0.500, and 1:0.250). The as-synthesized monoliths were carbonized (at 600 °C) and chemically activated with varying proportions of NaOH (1:1, 1:2, and 1:3). This materials offer the CO_2 adsorption effect under dynamic conditions, fast mass transfer, easy handling, and outstanding stability throughout the adsorption-desorption cycle. FE-SEM, and HR-TEM analyses confirmed the porous nature and shape of the adsorbents, while XPS examination revealed the presence of distinct functional groups on the surface of the monolith. By increasing the mass ratios (MGO:NaOH) from 1:1 to 1:2, the surface areas increased by approximately 2.6 times, ranging from 520.8 to 753.9 $m^2\ g^{-1}$ (surface area of the untreated MGO was 289.2 $m^2\ g^{-1}$). Consequently, this resulted in a notable enhancement of 2.10 mmol g^{-1} in dynamic CO_2 capture capacity. The assessment encompassed the evaluation of production yield, selectivity, regenerability, kinetics, equilibrium isotherm, and isosteric temperatures of adsorption (Q_{st}). The decrease in CO_2 capture effectiveness with rising adsorption temperature indicated an exothermic and physisorption process. The regenerability of 99.1 % at 100 °C and excellent cyclic stability with efficient CO_2 adsorption make this monolithic adsorbent appropriate for post-combustion CO_2 capture. The significant Q_{st} lend support to the heterogeneity of the adsorbent's surface, and the pseudo-second-order kinetic model along with the Freundlich isotherm model emerged as the most fitting. Therefore, the current investigation shows that the carbon-enriched adsorbents enhance the CO_2 adsorption capacity. It may be used as a low-cost pretreatment method on an industrial scale before carbon capture.

1. Introduction

The effects of CO_2 emissions cause global warming [1]. The combustion of fossil fuels and emissions, coupled with the extensive use of motor vehicles, has contributed to the escalation of climate change [2–4]. Hence, anthropogenic CO_2 emissions find application in various processes [5]. Thus, mitigating atmospheric CO_2 levels necessitates the deployment of CO_2 capture technologies. Amine adsorption stands out as a well-established method, making widespread use of CCS technology. Regrettably, the primary drawback of

* Corresponding author.
** Corresponding author.
E-mail addresses: hbhunia@thapar.edu (H. Bhunia), soumen.basu@thapar.edu (S. Basu).

https://doi.org/10.1016/j.heliyon.2024.e27439
Received 3 April 2023; Received in revised form 19 February 2024; Accepted 28 February 2024
Available online 2 March 2024

this adsorbent lies in the costs associated with regeneration studies [6]. As viable alternatives, CCS technology has been employed to capture CO_2 from solid adsorbents. Recently, a diverse range of solid adsorbents has been reported for the adsorption of CO_2 [7], likely activated carbon [8], Zeolite [9], silica [10]. In simpler terms, the CO_2 capture process brings out the solid sorbents of the monoliths, presenting a significant advantage. In general, monoliths are typically perceived as low-pressure flue gas conduits connected to an equivalent particle system [11–17] and rapid mass transfer [18–22]. Handling and transporting monoliths in powder form is more convenient [12], additionally, monoliths in powder form enhance structural characteristics [12,19]. Unlike metal-organic frameworks or zeolites, these monolithic nanomaterials demonstrate significant capacity for CO_2 capture. Carbon-based monolithic sorbents hold a higher potential, thanks to their suitability for repeated cycle processes [23]. The production of carbon-based monolith composites necessitates several stages involving high temperatures, focused energy, and precise pressure control [24–27].

Furthermore, a subset of monoliths undergoes post-production treatment with an acid or base to enhance their CO_2 adsorption capability [24,27,28]; the environmental concern, which poses a threat to the feasibility of scaling up, was not considered in either case. However, chemical activation is done by combining the chosen precursors with the necessary mass ratio of activating agents, such as KOH [29], K_2CO_3 [30], NaOH [31], H_2SO_4 [32], $ZnCl_2$ [33], subsequently carbonized under an inert environment, which results in a larger yield and the formation of porosity in the materials, by dehydrating the precursors and degradation their structural integrity. To attain activated carbons with specific characteristics, it is imperative to carefully control the activation temperature, duration, and heating rate during the production process. At this point, activated carbons are made from various carbon precursors through relevant activating agents [34]. NaOH is extensively used and recommended compared to other activators as it significantly amplifies porosity and specific surface area [35]. This study investigates the efficacy of chemically activated carbonization via NaOH treatment, with varying concentrations, in contrast to the previous method [36] of physical activation through UV-light exposure. The primary objective was to assess the impact of different activation techniques on the adsorption capabilities of monolithic adsorbents. Our findings suggest that the chemical activation process outperforms the physical activation method in terms of CO_2 adsorption capacity.

Here, we have described an environment-friendly technique and reduced carbon footmark for synthesizing carbon-rich MGO-based adsorbents for CO_2 capture. In this synthesis process, at 90 °C aqueous dispersion is employed to reduce graphene oxide by using oxalic acid (OxA) at different mass ratios. Conducting the chemical activation procedure involves combining the chosen precursors with the necessary mass ratio of the activating agent, sodium hydroxide (NaOH), and carbonizing the mixture at 600 °C within an inert environment. At the end of as-synthesized monoliths treated by NaOH, the well-developed surface area, CO_2 capture performance, and structural characteristics, particularly the porous morphology, were observed. The examination of surface chemistry and morphology relies on the optimization of reduction parameters to achieve an augmented surface area, refined material form, hierarchical morphology, and enhanced CO_2 absorption capability. We found that this synthesis procedure offers exceptional stability throughout adsorption-desorption cycles, even though there is a slight loss in CO_2 adsorption capacity during the cyclic operation. Then, the CO_2 adsorption was investigated under dynamic CO_2 adsorption. We have studied kinetics, isotherms, and thermodynamics of adsorption experiments. Three distinct kinetic models for CO_2 adsorption exist: Elovich, pseudo-first-order, and pseudo-second-order. Additionally, these kinetic models' reliability predicts that the CO_2 capturing capacity is easily retrieved by linear regression coefficient. The current study aims to manufacture inexpensive adsorbents from them via a straightforward and affordable way for CO_2 capture under dynamic conditions.

In this comprehensive article, we introduce a straightforward and scalable process for crafting monolithic adsorbents using chemically activated reduced graphene oxide. Subsequently, these materials spontaneously assemble, giving rise to three-dimensional graphene structures. This technique enables precise regulation of both shapes and pore density. The resulting materials exhibit exceptional selectivity, high pore volumes, and well-defined mesoporosity. Furthermore, we highlight the enhanced suitability of these adsorbents for CO_2 adsorption in post-combustion applications. The synthesized adsorbents demonstrate remarkable CO_2 capture capacity, highest CO_2 over N_2 adsorption selectivity, excellent cycling stability, rapid CO_2 removal rates and a moderately low initial Q_{st}.

2. Experimental

2.1. Materials

For synthesis, a diverse range of materials, including graphite powder, $NaNO_3$, H_2SO_4, $KMnO_4$, H_2O_2, HCl, $C_2H_2O_4$, and NaOH. In the pursuit of optimizing CO_2 capture performance, Sigma Gases & Services, based in New Delhi, India, supplied high-purity nitrogen gas with a concentration of 99.98%, along with carbon dioxide gases at concentrations of 50% and 20%.

2.2. Synthesis of monolithic reduced graphene oxide

Graphene oxide was synthesized using the modified Hummers' method [37]. The self-assembly process of graphene oxide was frequently employed in this synthesis [38]. GO aqueous dispersion with a specified concentration (5 mg/ml) was generated through 1 h of ultrasonication. After undergoing a 3-h stirring process at 90 °C, the system is cooled at 25 °C; the GO/OxA combination was prepared in various mass ratios (by weight) through the addition of oxalic acid. Specifically, the mixture was formulated at ratios of 1:1, 1:0.500, and 1:0.250. Subsequently, to achieve cohesive monolithic hydrogel, the homogeneous mixture underwent a 2-h hearing process at 90 °C. Following the preparation, the wet monolith underwent centrifugation to remove residual oxalic acid. To remove adsorbed water, the wet monolith underwent a final step of freeze-drying for 24 h at −55 °C and a pressure of 0.6 mbar, utilizing the HyperCOOL Cooling Trap HC3055 from Korea. Scheme 1 illustrates the synthesis process of the monoliths. Distinct names were

assigned to each synthesized MGOs as outlined in Table 1.

2.3. Synthesis of chemically activated adsorbent

The synthesis of chemically activated adsorbent was carbonized in successive processes [39–42]. The selected sample of MGO 0.250 was subjected to optimization at various temperatures, as documented in Table S2. The first process was to manually infuse MGO 0.250 with NaOH at varying weight ratios (MGO 0.250:NaOH = 1–3), then the mixture was dried for 12 h at 90 °C. The resultant prepared mixture was loaded on a clay boat and then located in the middle of the horizontally tubular furnace; after that ejected with N_2 (50 mL min^{-1}) for 10 min to blush out the air in the tubular furnace. Then, the samples were annealed at 600 °C with a ramping rate of 10 °C min^{-1} in the N_2 environment for 1 h. The prepared chemically activated samples were left to cool naturally at 25 °C; then, the samples were rinsed with a 5% HCl solution. DI-water, and dried in an oven for 12 h at 60 °C to get MGO 0.250 nanocomposites. By employing this method, chemically activated adsorbents were produced and designated distinct names were assigned to each synthesized MGO 0.250_x as detailed in Table 2. The resulting samples were identified as MGO 0.250_x, with x representing the activation ratio of NaOH. Production yield was determined using FPY method. The resulting MGO 0.250_2 adsorbent exhibited a production yield of 80.31%, as indicated in Table S7.

3. Results and discussion

3.1. Characterization of material

The reduction of graphene oxide through a self-assembly process with oxalic acid at 90 °C resulted in the formation of monoliths, with the structural foundation primarily composed of GO. The control over the rGO and its structural characteristics is contingent upon the reduction temperature, a parameter that concurrently dictates the dynamics of the graphene oxide (GO) reduction process. Graphene oxide (GO) platelets are extensively acknowledged for containing epoxy, hydroxyl (-OH), and carboxyl (-COOH) groups, which are subsequently eliminated during the reduction process [43]. This process develops a porous hierarchical morphology in monolithic structures in the above-illustrated process. As revealed in Table 1, these monolithic adsorbents show ultra-low density. The ultra-low density range of prepared monolithic adsorbents was 0.03–0.04 g^{-1} cm^3. The mass-to-volume ratio, employing a range of 15–20 mg for mass and 0.5 cm^3 for volume, was employed in the calculation of density. After treatment with OxA, the density of monoliths increases with the increase amount of OxA, indicating that these monoliths are more compact due to the quicker process.

Fig. 1(a) illustrates XRD patterns of GO, MGOs, and MGO 0.250_x samples. The (0 0 1), (0 0 2), and (1 0 0) crystal planes are denoted by distinctive diffraction peaks at 10.70°, 26.90°, and 42.75°, respectively of GO, MGOs, and MGO 0.250_x [36,44,45]. The

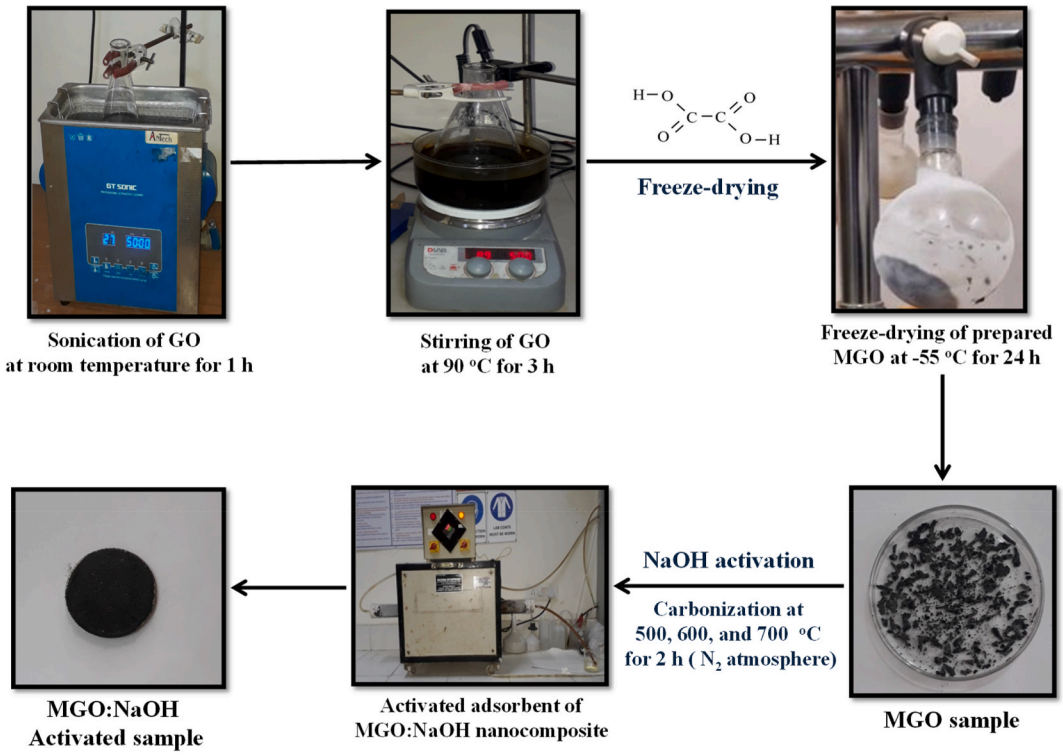

Scheme 1. Fabrication of monolithic adsorbents utilizing GO/rGO.

Table 1
Preparation process for MGO from GO:OxA (at ratios ranging from 1:0.250 to 1:1.000).

Samples name	GO: OxA	Temperature °C	Density (g^{-1} cm^3)
MGO 0.250	1: 0.250	90	0.030
MGO 0.500	1: 0.500	90	0.036
MGO 1.000	1: 1.000	90	0.040

Table 2
Chemical activation of MGO 0.250_x using different mass ratios of MGO 0.250 to NaOH.

Samples Name	Activation Time	Activation Temperature	MGO 0.250: NaOH (weight in mg)
MGO 0.250	-	-	-
MGO 0.250_1	1 h	600 °C	1:1
MGO 0.250_2	1 h	600 °C	1:2
MGO 0.250_3	1 h	600 °C	1:3

peak intensity slightly changes after carbonization at 600 °C for different mass ratios of MGO 0.250:NaOH; the peak intensity for MGO 0.250_1 (1:1) and MGO 0.250_3 (1:3) slightly decreases, whereas for MGO 0.250_2 (1:2) peak slightly increases. The discernment of this effect originates from the fluctuations in oxygen functionalities, marking the evident rise and subsequent decline in their presence, which was also confirmed from XPS survey scan analysis as revealed in Fig. 1(d). The distinctive crystal diffraction peaks presented at 26.10, 25.20, 25.50, and 25.83° for MGO 0.250, MGO 0.250_1, MGO 0.250_2, and MGO 0.250_3, respectively.

Raman spectral analysis of GO, MGOs, and MGO 0.250_x samples are revealed in Fig. 1(b). Occurrence of the adsorbent peaks at 1300 cm^{-1} and 1500 cm^{-1} can be attributed to the D and G bands [36,45–48]. The D and G bands virtually equalize in intensity for MGO 0.250, indicating a modest amount of crystal lattice defects produced by strong oxidation process, and helpful for creating MGOs [49]. The I_D/I_G ratio slightly increases after activation with the values of 1.02, 1.06, 1.07, 1.09, 1.24, 1.38, and 1.31 for GO, MGO 1.000,

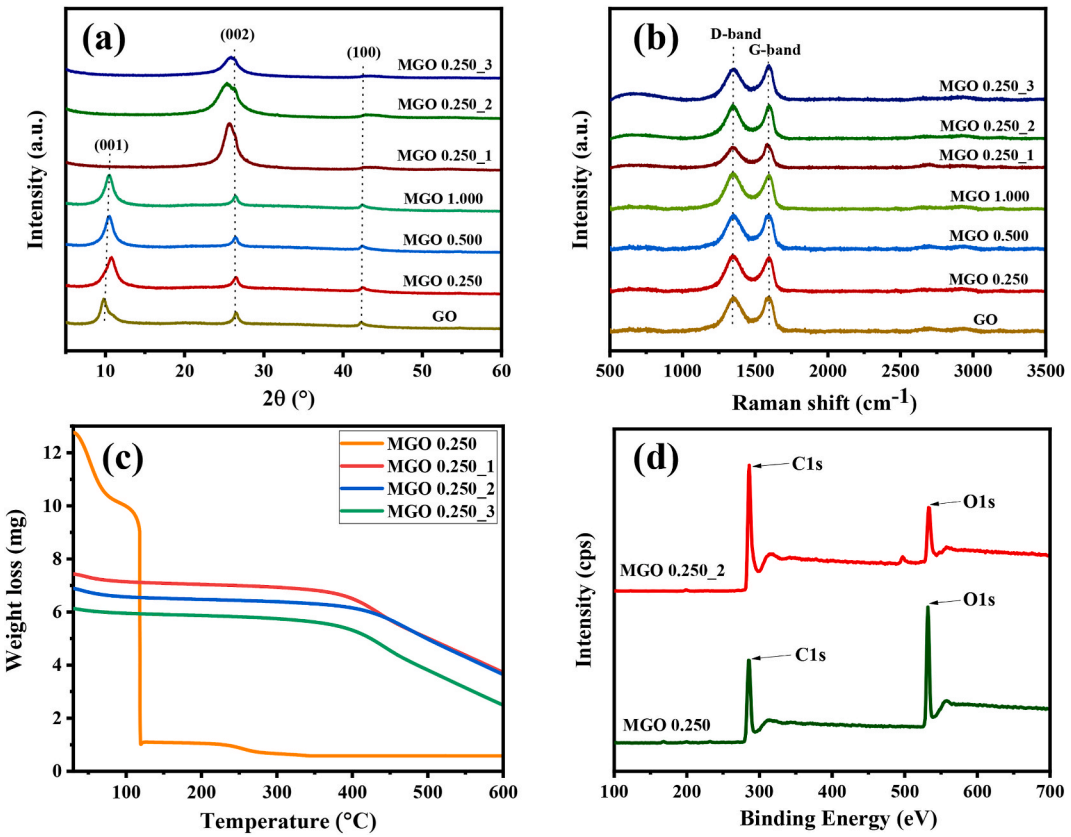

Fig. 1. (a) Wide-angle XRD patterns, (b) Raman spectra, (c) thermogravimetric analysis curves for MGO 0.250, MGO 0.250_x, and GO adsorbents, (d) along with X-ray photoelectron spectroscopy survey spectra of MGO 0.250 and MGO 0.250_2 adsorbents, were employed for the comprehensive characterization of GO, MGOs, and MGO 0.250_x adsorbents.

MGO 0.500, MGO 0.250, MGO 0.250_1, MGO 0.250_2, and MGO 0.250_3 respectively. The rising I_D/I_G ratio serves as an indicative measure of the degree of disorder, with the presence of edges, ripples, and faults emerging as substantial contributing factors [50]. This may be due to the attack of NaOH on the oxygenic defect regions, which decreases the O/C atomic ratios of the adsorbents.

Fig. 1(c) shows the Thermogravimetric Analysis (TGA) curves for both MGO 0.250 and NaOH-activated MGO 0.250. The MGO 0.250 experiences loses weight at 120 °C, ascribed to the presence of residual oxygen functional groups on its surface. After that, activated MGO 0.250 exhibits weight loss occurring between 400 °C and 600 °C, Most likely due to the oxygen in the samples being oxidized and decomposed. The weight loss is in the following order: MGO 0.250 > MGO 0.250_1> MGO 0.250_3 > MGO 0.250_2. It was observed that MGO 0.250_2 is the most thermally stable adsorbent.

Surface functionalities and O/C ratios of the synthesized adsorbents were determined through XPS analysis. Curves with binding energies approximately at 284.55–284.81 eV (C1), 284.96–285.24 eV (C2), 285.38–286.64 eV (C3), and 287.16–287.67 eV (C4) were employed for deconvoluting the C1s peak, depicted in Fig. 2(a–c) [51–54]. In the case of MGO 0.250 and MGO 0.250_2, the C/O ratio experienced an increase from 1.919 to 2.901, attributed to the removal of various oxygen groups during NaOH activation, as depicted in Fig. 1(d). Curves with binding energies approximately at 531.10–532.16 eV (O1), 532.76–533.46 eV (O2), and 533.12–534.90 eV (O3) were employed for deconvoluting the O1s peak, depicted in Fig. 2(b–d) [52–54]. Table S4 reveals a notable relative area % for the O2, O3, and wear track surface chemical shifts in MGO 0.250_2, underscoring their significance [45,55,56].

Characterization through FE-SEM imaging aimed to collect information pertaining to porosity, surface morphology, and the monolith structure. Leveraging the FE-SEM image, an examination of the surface morphology of MGOs and MGO 0.250_x were conducted, as illustrated in Fig. 3. Research tends to prioritize the investigation of porous morphology, given the lower presence of OxA and the more discernible pores. Notably, the activation of MGO 0.250 with NaOH weight ratios ranging from 1:1 to 1:3 resulted in a discernible improvement in surface roughness. The resulting MGO 0.250_2 adsorbent exhibited morphological disorders, as depicted in SEM and HR-TEM images presented in Fig. 4 [36,45,57,58]. When the water contact angle was more significant than (>90°), the MGO 0.250_x displayed poor wetting, while a slight contact angle (<90°) corresponds to larger surface wetting [59]. From Fig. 3, the FE-SEM image observations connected to an increase in surface roughness after NaOH activation was also seen in these images. Contrastingly, it manifests a planar yet twisted shape, suggesting the influence of NaOH in augmenting the pore structure and consequently modifying the morphology of the graphene layers [60].

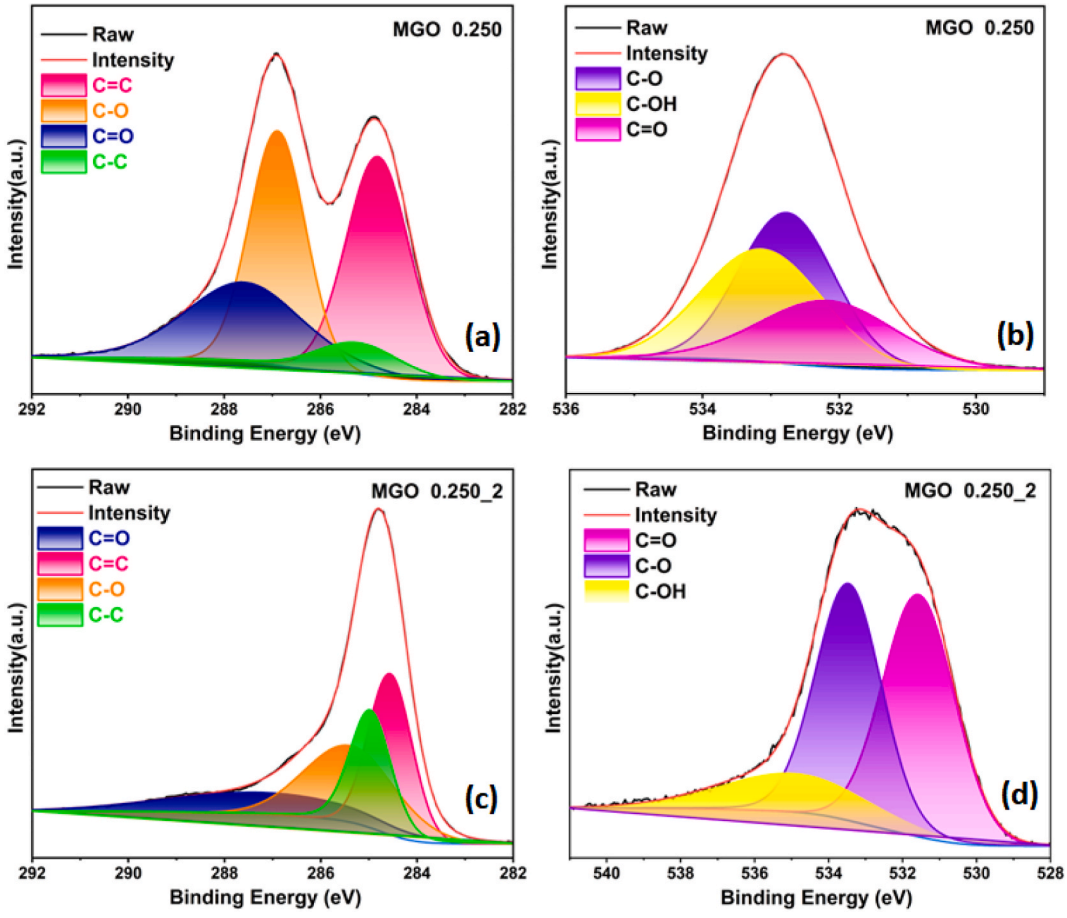

Fig. 2. XPS spectrum peak of C1s in Fig. 2(a, c) and O1s in Fig. 2(b, d).

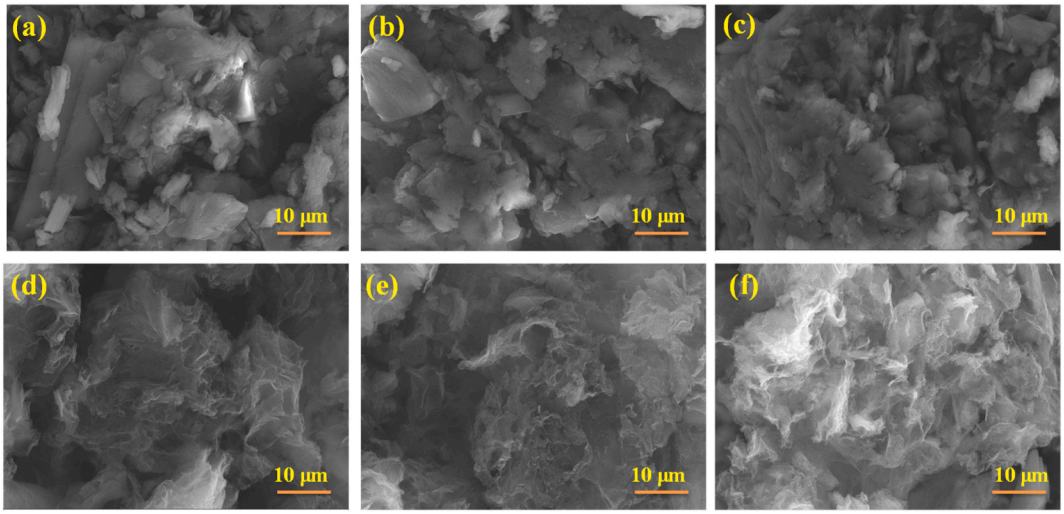

Fig. 3. Adsorbents are depicted in the FE-SEM images: (a) MGO 1.000, (b) MGO 0.500, (c) MGO 0.250, (d) MGO 0.250_1, (e) MGO 0.250_2, and (f) MGO 0.250_3.

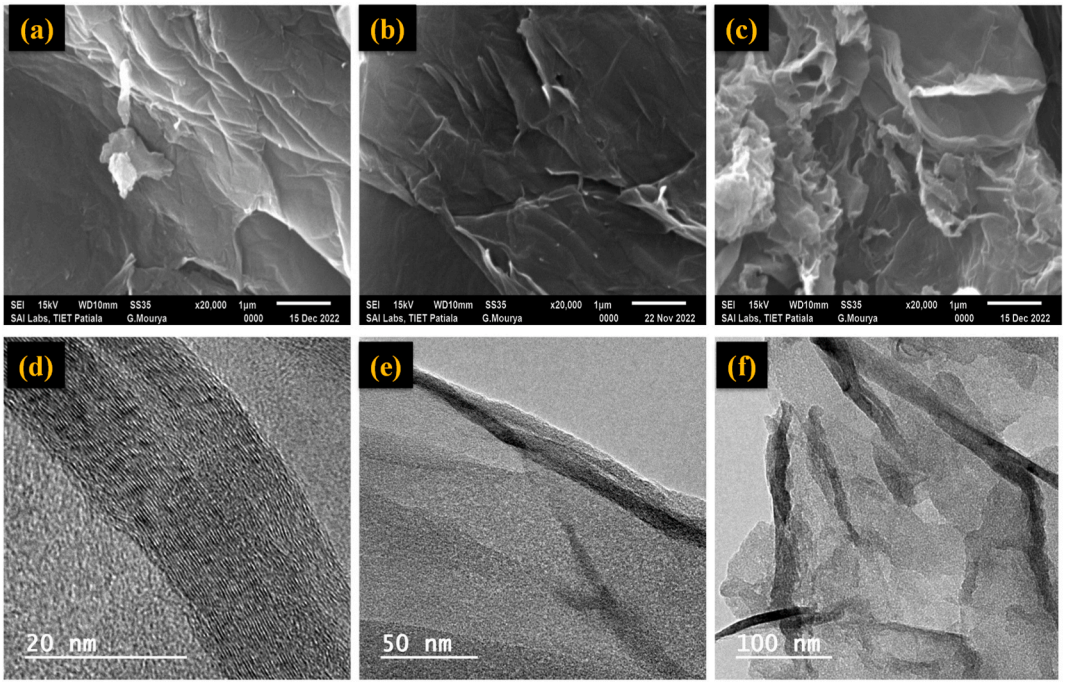

Fig. 4. SEM images of (a) GO, (b) MGO 0.250, (c) MGO 0.250_2, and (d to f) HR-TEM image of MGO 0.250_2.

The N_2 adsorption isotherms and the corresponding adsorption-desorption curve, is illustrated in Fig. 5(a)–and as indicated in Table S1. Type-IV isotherms affirm the mesoporous character with pore diameter ranging between 5.0 and 20.0 nm. This study investigates the augmentation of specific surface area (SSA) subsequent to NaOH treatment. This phenomenon is likely attributed to the heightened porosity, which is particularly prominent in MGO 0.250_2, boasting the surface area of 753.9 $m^2\ g^{-1}$ and total pore volume of 1.97 $cm^3\ g^{-1}$. Despite certain MGO 0.250_x samples exhibiting surface areas considerably smaller than the projected 2630 $m^2\ g^{-1}$ for an individual graphene sheet, our findings remain noteworthy [61]. Nevertheless, these values surpass those of graphene aerogel, which stands at 512 $m^2\ g^{-1}$ [62], graphene sponge at 418 $m^2\ g^{-1}$ [63], and graphene nanoplates at 480 $m^2\ g^{-1}$ [64]. Fig. 5(b) illustrates the PSDs obtained through the BJH method, highlighting that the predominant portion of the pore volume is attributed to apertures with a diameter below 20 nm. Notably, a distinct PSDs emerges within the 5–16 nm range, signifying the presence of small mesopores across all MGOs in the basal plane. MGO 0.250_2 exhibits a more densely packed structure, as evidenced by Table S1. The shift in the

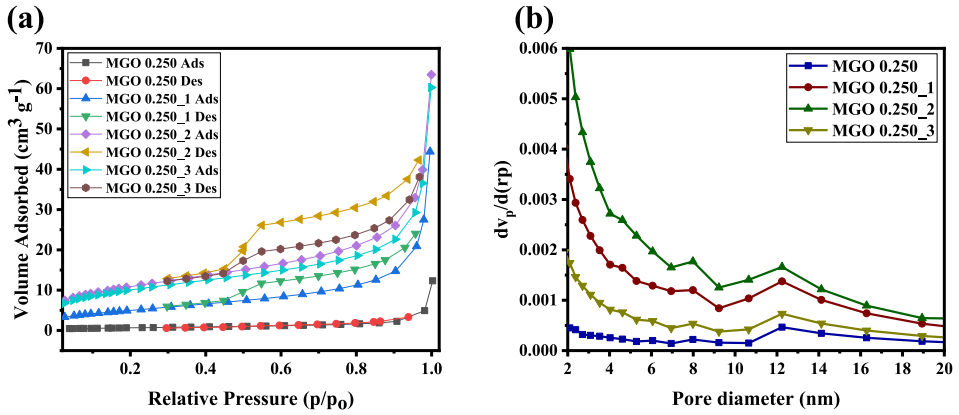

Fig. 5. (a) N_2 adsorption-desorption isotherm curves, while (b) displays the pore size distribution curves.

maximum of the pore size distribution PSDs, transitioning from 3.59 nm for MGO 0.250_3 to 3.95 nm for MGO 0.250_2, suggests that elevating NaOH levels resulted in the formation of MGO with larger pores. Adjusting the MGO 0.250 to NaOH ratios conveniently allows for the concurrent modulation of the samples' porosity.

3.2. CO_2 adsorption performance

Fig. 6(a and b) presents the assessment of CO_2 adsorption capacity for MGOs, and MGO 0.250_x. The precise CO_2 adsorption values for the optimized conditions are detailed in Table S2 and Table S3. The MGO 0.250_2 adsorbent attains its peak in the initial stage, the former exhibits a CO_2 capture capacity of approximately 2.10 mmol g^{-1}, surpassing the latter by about 2.6 times, as the former's capacity. The gaps created by graphene's layer-by-layer self-assembly process may be responsible for some of the CO_2 adsorptions on MGOs. In addition, all the MGOs showed sharp increase in CO_2 capture performance [65]; therefore, accessing all of the MGOs pores was possible. Furthermore, the pressure range's isotherm under investigation did not show an apparent plateau. The ascending order of equilibrium CO_2 absorption at 25 °C and pressure 1 bar as follows: MGO 0.250_1 with 1.20 mmol g^{-1}, followed by MGO 0.250_3 with 1.71 mmol g^{-1}, and MGO 0.250_2 leading with the highest capacity at 2.10 mmol g^{-1}. MGO 0.250_2 emerged as the optimal candidate, showcasing the highest surface area, and optimal CO_2 adsorption performance. The literature also outlines the facilitation of low-pressure CO_2 adsorption through smaller pores [66].

Moreover, Table 3 indicates that MGO 0.250_2's CO_2 adsorption capability is similar to other graphene-based and carbonaceous materials at identical temperatures. increase in adsorption temperature from 25 °C to 50 °C, the amount of CO_2 adsorbed on MGO 0.250_2 decreased from around 2.10 mmol g^{-1} to approximately 1.35 mmol g^{-1}. It is anticipated that the exothermic nature of adsorption will contribute to reduction in CO_2 adsorption at 50 °C.

An investigation of the regeneration process for the activated adsorbents at four distinct temperatures (25, 50, 75, and 100 °C) is illustrated in Fig. 7(a). As highlighted in Table 5, CO_2 recovery % experienced an increase with NaOH treatment, a phenomenon that was validated across a range of temperatures [67]. This effect is envisaged to occur by averting the entrapment of CO_2 within the MGO

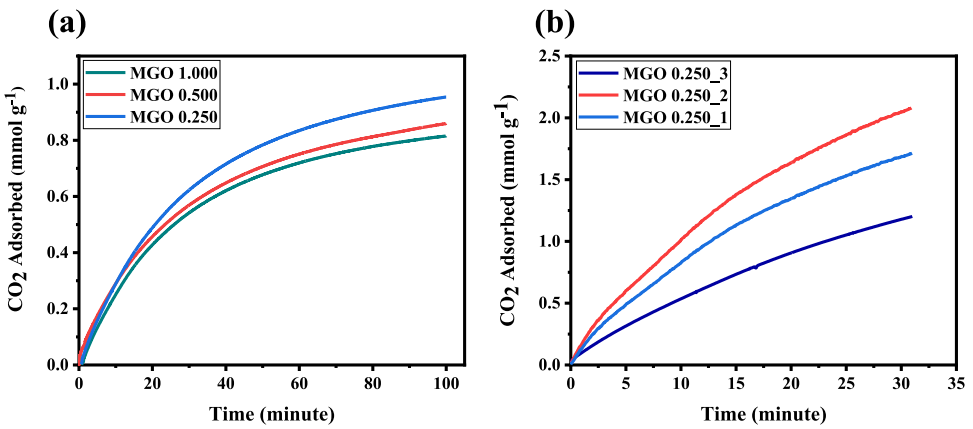

Fig. 6. CO_2 capture performance of (a) MGOs and (b) MGO 0.250_x at 25 °C.

Table 3
Comparing CO_2 adsorption performance between MGO 0.250_2 and other adsorbents.

Adsorbent	Activation method	Experimental conditions		CO_2 Adsorbed (mmol g-1)	Ref.
		CO_2 conc. (%)	Temp. (°C)		
MGO 0.250_2*	Chemical/NaOH (600 °C)	50	25	2.10	Present study
MGO 0.250_2*	Chemical/NaOH (600 °C)	50	50	1.35	Present study
3D graphene	Chemical/NaOH (500 °C)	50	25	1.71	[68]
HPGC-850	Chemical/(850 °C)	100	0	1.76	[69]
PAN-KOH	Chemical/KOH (800 °C)	12.5	30	1.20	[70]
Carbon monolith	Chemical/KOH (25 °C)	15	30	0.66	[71]
EDA	Chemical/COOH (85 °C)	100	25	2.00	[72]
N-containing resin	Chemical/K_2CO_3 (700 °C)	100	25	1.90	[73]
HGF-II	Chemical/HNO_3 (500 °C)	100	25	1.40	[39]
WT-550-2	Chemical/KOH (550 °C)	10	25	4.54	[40]
MCF-700-0.2	Chemical/KOH (700 °C)	10	25	3.30	[41]
PHS-650-3	Chemical/KOH (650 °C)	10	25	4.18	[42]

multilayer galleries, as reported by the active sites and demonstrated through the presented XRD data.

Fig. 7(b) depicts the successive adsorption-desorption cycles of the adsorbent, with adsorption occurring at 25 °C and desorption at 150 °C. MGO 0.250_2 consistently exhibits adsorption of nearly 2.10 mmol g^{-1} throughout multiple adsorption-desorption cycles, without any noticeable efficiency reduction. The desorption of CO_2 necessitates approximately 1.18 MJ of heat energy per kilogram of CO_2, as per the calculations provided in the (SI-file). Following numerous cycles, the CO_2 uptake remained consistently constant for MGO 0.250_2, showcasing its exceptional regenerability and cyclic stability outlined in Table 4. Due to the presence of metastable states between the sorbate and sorbent, the pressure falls below the thermodynamic equilibrium, signifying that MGO 0.250 encounters challenges in releasing the adsorbed CO_2 [74]. These findings underscore the advantage of treating MGOs with NaOH to facilitate the displacement of adsorbed CO_2.

Produced adsorbents were employed in selectivity tests at 25 °C, and influence of NaOH activated adsorbent revealed in Fig. 8(a). Significant decrease in N_2 adsorption is observed upon NaOH activation, as indicated by the results for MGO 0.250_2 on NaOH activated adsorbents. In contrast to MGO 0.250 at 1 bar, the selectivity of MGO 0.250_2 experienced an approximately 3.7-fold increases, this enhancement can be attributed to the improved CO_2 uptake. Table S6 reveals the outcomes of this study. For MGO 0.250_1, MGO 0.250_2, and MGO 0.250_3, selectivity values of 17.15, 35.00, and 34.20 were respectively recorded at 1 bar. According to the study's findings, the MGO 0.250_2 adsorbent is a great substitute for CO_2 recovery from flue gases [3,39,70,75].

Fig. 8(b) presents the breakthrough curves; evaluating the CO_2/N_2 binary gas mixture with a 50% CO_2 flowing at 25 °C and 1 bar pressure. The dynamic CO_2 adsorption capacity is approximately 1.0 mmol g^{-1}. CO_2 was observed to emerge in the effluent after certain duration, whereas N_2 was promptly detected. This demonstrates that N_2 can't adsorb as well as CO_2. Initially, the active sites of the adsorbent are predominantly occupied by N_2, as evidenced of C/C_o for $N_2 > 1$. Nevertheless, as time progresses, there is a gradual displacement of N_2 by CO_2, highlighting the adsorbent's stronger affinity for CO_2 [70,75].

3.3. CO_2 adsorption kinetic studies

In operational conditions with a pressure of 1 atm, temperatures ranging from 25 to 50 °C, and CO_2 flow concentrations varying

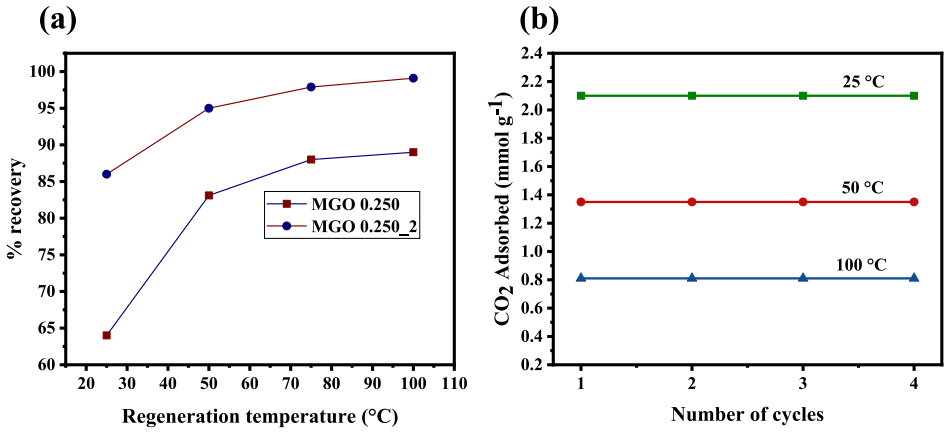

Fig. 7. (a) Regeneration of MGO 0.250, MGO 0.250_2 adsorbents and (b) MGO 0.250_2 adsorbent underwent repeated cycles of CO_2 uptake at 25 °C, 50 °C, and 100 °C.

Table 4
Cycle of adsorption-desorption for adsorbents MGO 0.250 and MGO 0.250_2.

Adsorbent	CO_2 Adsorbed (mmol g^{-1}) at 25 °C	CO_2 Desorbed (mmol g^{-1})				Recovery % of Adsorbed CO_2			
		25 °C	50 °C	75 °C	100 °C	25 °C	50 °C	75 °C	100 °C
MGO 0.250	0.95	0.60	0.79	0.83	0.84	63.1	83.1	87.3	88.4
MGO 0.250_2	2.10	1.81	1.99	2.06	2.08	86.1	94.7	98.0	99.1

Table 5
Thermodynamic parameters (ΔG^o, ΔH^o, ΔS^o) of MGO 0.250_2 adsorbent.

Thermodynamic parameter of CO_2 adsorption						Isosteric heat of adsorption	
Adsorbent	Temp (K)	K_d	ΔG^o (KJ mol^{-1})	ΔH^o (KJ mol^{-1})	ΔS^o (JK^{-1} mol^{-1})	q_e (mmol g^{-1})	Q_{st} KJ mol^{-1}
MGO 0.250_2	298	0.048	−1.1189234	−11.1564133	+4.7370520	0.20	25.3
	303	0.182	−4.4584838			0.4	27.9
	313	0.336	−7.8743667			0.6	30.4
	323	0.470	−13.2621483			0.8	35.0
						1.0	37.2
						1.2	39.8
						1.4	41.0

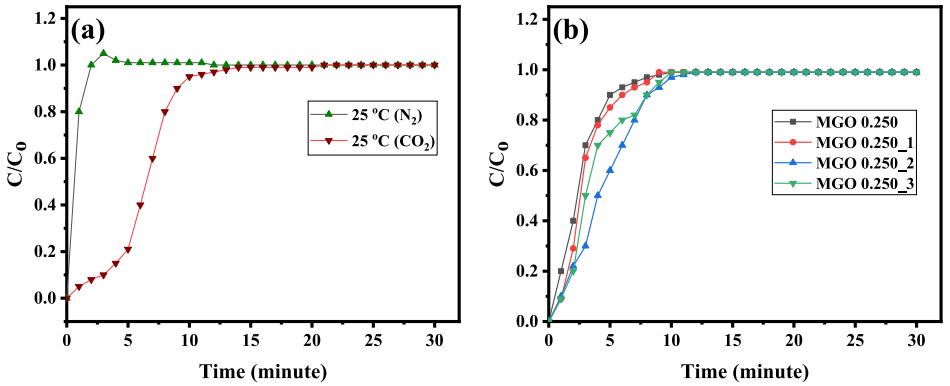

Fig. 8. (a) CO_2/N_2 selectivity curve of MGO 0.25_2 adsorbent and (b) breakthrough curves showing MGO 0.250 and MGO 0.250_x adsorbents.

between 50% and 20%, the MGO 0.250_2 demonstrates enhanced CO_2 adsorption kinetics, exhibiting a faster rate of adsorption. Fig. 9 (a and b) depicts significant CO_2 uptake occurring at elevated maximum of 94% CO_2 adsorption. This observation aligns more closely with the outcomes of previous experiments, reinforcing the consistency of the findings [39,40,42,75]. Diffusional constraints were suggested to be the cause of the sample's enhanced oxygen functionality and its propensity for quick adsorption. Consequently, the physisorption type of fitting, such as by van der Waals interaction, is revealed by MGO 0.250_2 [76]. These results unequivocally establish the capability of MGO 0.250_2 to operate with exceptionally short adsorption/desorption cycle lengths, presenting a notable economic advantage for commercial deployment. This material effectively demonstrates its potential in separating CO_2 from flue gases. In order to determine the adsorption rate and the asorbent's capacity to adsorb a larger amount of adsorbate, adsorption kinetic studies are necessary [77], the formula provided in Equations S8, S9, and S10. Various kinetic models have been explored in this experimental study, as illustrated in Fig. 9(a and b). Because of the lower error percentage (%) and higher R^2 values observed, adhered to the pseudo-second-order kinetic model. This model is identified as more suitable compared to other models, as demonstrated in Table S8.

3.4. CO_2 adsorption isotherm studies

The determination of the adsorption mechanism and the elucidation of the roles played by the CO_2 adsorption procedure were achieved through an adsorption isotherm analysis. In this investigation, we employed Equations S12, S13, and S14 to detail the fitting of isotherm models—Langmuir, Freundlich, and Temkin to experimental CO_2 adsorption data. The computed and experimental R^2 values for various isotherm models are demonstrated in Table S9. As depicted in Fig. 10(a), the superior R^2 values affirm Freundlich isotherm model. This model is identified as more suitable compared to other models. Adsorbent surface heterogeneity is illustrated employing the Freundlich isotherm model. The optimum value for CO_2 adsorption at low temperatures is suggested by the K_F values (n

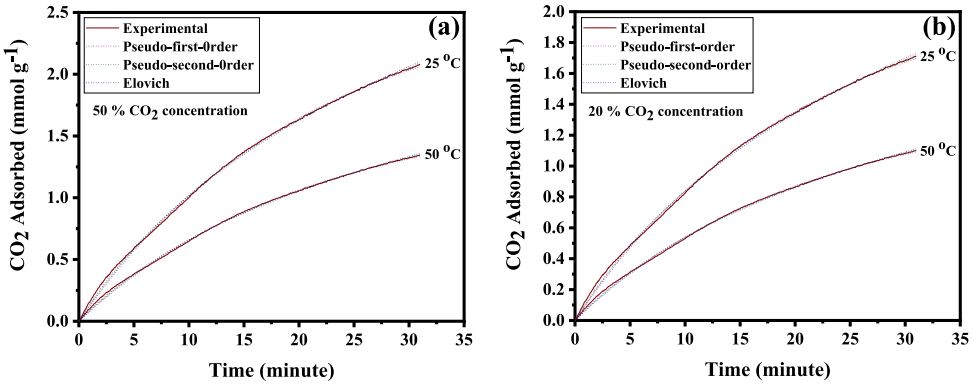

Fig. 9. Experimental data fitting with kinetic models: (a) 50 % CO_2 concentration flow of MGO 0.250_2 adsorbent, and (b) 20 % CO_2 concentration flow of MGO 0.250_2 adsorbent.

< 1) [78]. The Freundlich model for MGO 0.250_2 adsorbent best fits experimental data with higher R^2 values, as observed in Table S9.

3.5. *Thermodynamic studies*

The determination of thermodynamic parameters crucially hinges on the interaction between CO_2 and the adsorption sites on the adsorbent surface during the CO_2 adsorption process. Equation (1) was used to measure the ΔG°, whereas ΔS°, ΔH° in KJ mol^{-1} can be determined through the Vant Hoff plot and Equation S16 [79], and the Q_{st} by Equation S17 [80]. Table 5 and Table S10 show calculated values of thermodynamic factors. The negative value of ΔH° (-11.1564133 kJ mol^{-1}), show the process is exothermic; and other hand, the value of ΔH° lies in the range between $< \pm$ 20 kJ mol^{-1} show the nature is predominantly physisorption [80]. Moreover, negative ΔG° values show the adsorption process is spontaneity, and feasibility [78]. The positive ΔS° values ($+4.7370520$ JK^{-1} mol^{-1}) suggests an increased affinity of adsorbents, indicating a rise in randomness or disorder at the solid/gas surface. Utilizing Equation (2), the Q_{st} values for MGO 0.250_2 was calculated at different q_e, ranging from 25.3 kJ mol^{-1} to 41.0 kJ mol^{-1}, with an average of approximately 33.8 kJ mol^{-1}, as detailed in Table 5. On the other hand, the isosteric heat of the activated adsorbent increased significantly, especially with higher CO_2 loadings, it reached approximately 41.00 kJ mol^{-1}. The adsorbed CO_2 molecules demonstrate strong lateral interactions with one another are responsible for this behavior, according to Fowler-Guggenheim model [81], which explains the interaction energy between the molecules. This phenomenon is further substantiated by the existence of intermolecular forces on the substandard graphene surface [82]. Recent investigations on CO_2 adsorption by carbonaceous materials have also reported a similar relationship between isosteric temperatures of adsorption and surface coverage [70,83,84].

The Q_{st} values were measured at various temperatures, revealing fluctuations in randomness and disorder. The increase in surface coverage aligns with the heterogeneous behavior of the surface adsorption sites of MGO 0.250_2. Moreover, in comparison to reported values ranging from 28.40 to 10.50 kJ mol^{-1} for different samples, the Q_{st} values are more significant [85], signifying the stronger

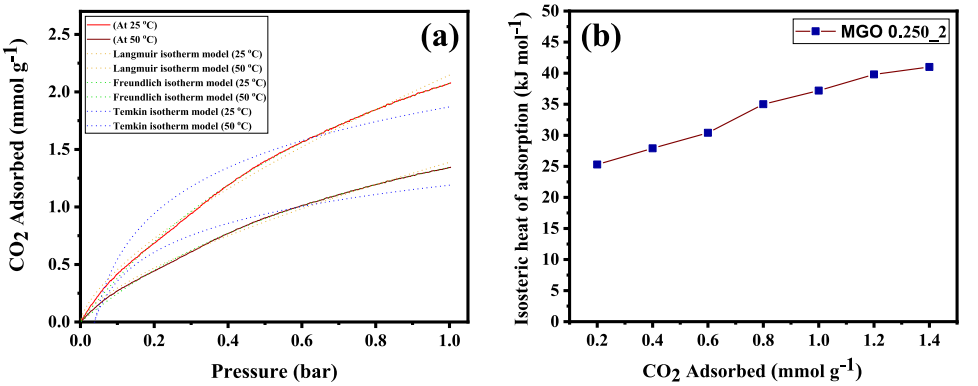

Fig. 10. (a) Experimental data fitting with isotherm model at 25 °C, 50 °C of MGO 0.250_2 adsorbent and (b Plot of Q_{st} values on MGO 0.250_2 adsorbent verses q_e for CO_2 adsorption.

attraction toward CO_2 heat of adsorption. A graph is plotted Q_{st} against 1/T (K^{-1}), as shown in Fig. 10(b).

$$\Delta G^0 = -RTlnK_d \tag{1}$$

$$\ln(P) = -\frac{\Delta H}{RT.} + C \tag{2}$$

3.6. Mechanism of CO_2 capture performance enhancement

The physiochemical, thermodynamic, and kinetic characteristics plays a pivotal role in shaping the approach for CO_2 capture. The size and shape of the pores are critical factors, and their abundance is essential for the effective functioning of the CO_2 capture mechanism. Furthermore, a high CO_2 adsorption rate requires an adsorbent with a large volume and surface area of pores. A parallel increase in the percentage of mesopores is observed in Fig. S1(a) as CO_2 adsorption capability rises. The primary reason for the increase in CO_2 adsorption is the proportional rise in mesopores, which ranges from 66.66 to 78.68 % outlined in Table S1. According to Figs. S1 (b and c), the d < 1 nm range exhibits the best linear connection ($R^2 = 0.996$), with a higher R^2 value than the d > 1 nm range.

By utilizing FT-IR spectra, we successfully identified individual adsorption peaks, as depicted in Fig. S2(b). The corresponding assignments for these peaks are detailed in Table S5. Significant variations were observed between the two spectra in the 1600 to 1200 cm^{-1} range. Table S5 and Fig. S2 present the outcomes of our efforts to isolate the spectra for a more comprehensive analysis of the 1600 to 1200 cm^{-1} range. The existence of HCO_3^- recommended the development of bicarbonate, whereas the peak equivalent to COO^- showed the development of carbamate. These results lend support to the notion that π-π interactions can facilitate the self-assembly of 2D porous graphene into a 3D hierarchical porous graphene [57,58]. Furthermore, the wetting properties of MGO 0.250_x were evaluated based on the water contact angle calculation [59]. Furthermore, in comparison to MGOs, MGO 0.250_x displayed larger interlayer spaces, evident from the slight shift in the (002) diffraction peaks as illustrated in the XRD patterns presented in Fig. 1(a). Consequently, this contributed to the augmentation of the surface area and an increase in adsorption capacity, as outlined in Table S1.

Unveiling the thermodynamic parameters and elucidating the intricacies of CO_2 interaction with the adsorbent surface are indispensable for a thorough comprehension of the CO_2 adsorption mechanism. In our investigation, as the adsorption temperature increased, we observed a decrease in capture performance, indicating an exothermic and physisorption-based adsorption process, as illustrated in the Table 5 and Table S10. The confirmation of an exothermic nature is evident from the of ΔH° (-11.1564133 kJ mol^{-1}), providing robust support for its physisorption-based mechanism [80]. Furthermore, as depicted in Fig. 9, the ΔG° was determined to be relatively higher, indicating an accelerated rate of the reaction [82]. The CO_2 adsorption exhibited exceptional rates, reaching peak of 94% CO_2 adsorption. The aforementioned observation suggests that the heightened reactivity of oxygen functionality, as illustrated in Fig. 2(d), contributed to an accelerated reaction rate, thereby enhancing the probability of rapid adsorption. It's crucial to highlight that the rapid adsorption could potentially be attributed to diffusion constraints within the system. With van der Waals interactions acting as the primary driving force, MGO 0.250_2 thus exhibits a physisorption-based process [76].

4. Conclusions

In this investigation, CO_2 adsorption efficiency of the developed MGO-based adsorbents was assessed across various parameters, including temperature, different concentrations of CO_2, and a constant pressure of 1 bar. Specifically, MGO 0.250_2 stands out as the optimal adsorbent, showcasing an enhanced capacity for maximum CO_2 adsorption. We observed that MGO 0.250_2 activated adsorbent gives the best CO_2 adsorption of 2.10 mmol g^{-1} due to having higher surface areas of 753.9 m^2 g^{-1}. Moreover, in the case of MGO 0.250 and MGO 0.250_2, the regeneration study performed at 100 °C demonstrated an enhancement in the recovery % increasing from 86.40% to 90.10%. This indicates a rapid desorption process post-adsorption, with a consistently stable adsorption capacity observed throughout the adsorption-desorption cycles. With its lower error percentage (%) and higher R^2 values, the kinetic experiments confirmed the excellent fit of the pseudo-second-order model. Similarly, the elevated R^2 value of the Freundlich model suggests that it is the most fitting model in the isotherm investigations as well. Furthermore, the thermodynamic parameters confirm that the characteristic nature of the adsorption is physisorption. The dynamic CO_2 capture capacity of MGO 0.250_2, surpassing 1 mmol g^{-1}, positions it as a promising candidate for industrial applications.

Data availability statement

The data will be made available on request.

Funding statement

This research did not receive any specific grant from funding agencies.

CRediT authorship contribution statement

Ranjeet Kumar Jha: Data curation, Investigation, Methodology, Software, Validation, Visualization, Writing – review & editing.

Haripada Bhunia: Conceptualization, Formal analysis, Investigation, Methodology, Resources, Supervision, Visualization, Writing – original draft. **Soumen Basu:** Conceptualization, Data curation, Formal analysis, Investigation, Methodology, Supervision, Visualization, Writing – original draft, Writing – review & editing.

Declaration of competing interest

The authors declare that they have no known competing financial interests or personal relationships that could have appeared to influence the work reported in this paper.

Acknowledgments

The authors want to acknowledge the Thapar Institute of Engineering and Technology, Patiala, Punjab (India), for providing instrumental and financial support. We are thankful to the DCBC, ChED, SPMS, CEEMS-Lab, TIET, Patiala for the help with sample characterization, i.e., XRD, FE-SEM, SEM, Raman spectra, TGA, BET, etc., and Sprint Testing Solutions Nagpur, India for the help with sample characterization, i.e., XPS, and HR-TEM.

Appendix A. Supplementary data

Supplementary data to this article can be found online at https://doi.org/10.1016/j.heliyon.2024.e27439.

References

[1] M.Z. Jacobson, Review of solutions to global warming, air pollution, and energy security, Energy Environ. Sci. 2 (2009) 148–173, https://doi.org/10.1039/B809990C.
[2] M.R. Raupach, G. Marland, P. Ciais, C. Le Quéré, J.G. Canadell, G. Klepper, C.B. Field, Global and regional drivers of accelerating CO 2 emissions, Proc. Natl. Acad. Sci. USA 104 (2007) 10288–10293, https://doi.org/10.1073/pnas.0700609104.
[3] A.M. Varghese, K.S.K. Reddy, S. Singh, G.N. Karanikolos, Performance enhancement of CO2 capture adsorbents by UV treatment: the case of self-supported graphene oxide foam, Chem. Eng. J. 386 (2020) 124022, https://doi.org/10.1016/j.cej.2020.124022.
[4] L.A. Darunte, A.D. Oetomo, K.S. Walton, D.S. Sholl, C.W. Jones, Direct air capture of CO 2 using amine functionalized MIL-101(Cr), ACS Sustain. Chem. Eng. 4 (2016) 5761–5768, https://doi.org/10.1021/acssuschemeng.6b01692.
[5] S. Zulfiqar, S. Awan, F. Karadas, M. Atilhan, C.T. Yavuz, M.I. Sarwar, Amidoxime porous polymers for CO2 capture, RSC Adv. 3 (2013) 17203, https://doi.org/10.1039/c3ra42433b.
[6] D.Y.C. Leung, G. Caramanna, M.M. Maroto-Valer, An overview of current status of carbon dioxide capture and storage technologies, Renew. Sustain. Energy Rev. 39 (2014) 426–443, https://doi.org/10.1016/j.rser.2014.07.093.
[7] J.W. Maina, C. Pozo-Gonzalo, L. Kong, J. Schütz, M. Hill, L.F. Dumée, Metal organic framework based catalysts for CO 2 conversion, Mater. Horizons. 4 (2017) 345–361, https://doi.org/10.1039/C6MH00484A.
[8] R.S. Franchi, P.J.E. Harlick, A. Sayari, Applications of pore-expanded mesoporous silica. 2. Development of a high-capacity, water-tolerant adsorbent for CO 2, Ind. Eng. Chem. Res. 44 (2005) 8007–8013, https://doi.org/10.1021/ie0504194.
[9] T.-H. Bae, M.R. Hudson, J.A. Mason, W.L. Queen, J.J. Dutton, K. Sumida, K.J. Micklash, S.S. Kaye, C.M. Brown, J.R. Long, Evaluation of cation-exchanged zeolite adsorbents for post-combustion carbon dioxide capture, Energy Environ. Sci. 6 (2013) 128–138, https://doi.org/10.1039/C2EE23337A.
[10] M.A. de la Casa-Lillo, F. Lamari-Darkrim, D. Cazorla-Amorós, A. Linares-Solano, Hydrogen storage in activated carbons and activated carbon fibers, J. Phys. Chem. B 106 (2002) 10930–10934, https://doi.org/10.1021/jp014543m.
[11] B. Crittenden, A. Patton, C. Jouin, S. Perera, S. Tennison, J.A.B. Echevarria, Carbon monoliths: a comparison with granular materials, Adsorption 11 (2005) 537–541, https://doi.org/10.1007/s10450-005-5981-9.
[12] A. Arami-Niya, T.E. Rufford, Z. Zhu, Activated carbon monoliths with hierarchical pore structure from tar pitch and coal powder for the adsorption of CO2, CH4 and N2, Carbon N. Y. 103 (2016) 115–124, https://doi.org/10.1016/j.carbon.2016.02.098.
[13] W.Y. Hong, S.P. Perera, A.D. Burrows, Manufacturing of metal-organic framework monoliths and their application in CO 2 adsorption, Microporous Mesoporous Mater. 214 (2015) 149–155, https://doi.org/10.1016/j.micromeso.2015.05.014.
[14] D.P. Vargas, M. Balsamo, L. Giraldo, A. Erto, A. Lancia, J.C. Moreno-Piraján, Equilibrium and dynamic CO 2 adsorption on activated carbon honeycomb monoliths, Ind. Eng. Chem. Res. 55 (2016) 7898–7905, https://doi.org/10.1021/acs.iecr.5b03234.
[15] H. Thakkar, S. Eastman, A. Hajari, A.A. Rownaghi, J.C. Knox, F. Rezaei, 3D-Printed zeolite monoliths for CO 2 removal from enclosed environments, ACS Appl. Mater. Interfaces 8 (2016) 27753–27761, https://doi.org/10.1021/acsami.6b09647.
[16] D. Qian, C. Lei, G.-P. Hao, W.-C. Li, A.-H. Lu, Synthesis of hierarchical porous carbon monoliths with incorporated metal–organic frameworks for enhancing volumetric based CO 2 capture capability, ACS Appl. Mater. Interfaces 4 (2012) 6125–6132, https://doi.org/10.1021/am301772k.
[17] Y. Jin, S.C. Hawkins, C.P. Huynh, S. Su, Carbon nanotube modified carbon composite monoliths as superior adsorbents for carbon dioxide capture, Energy Environ. Sci. 6 (2013) 2591, https://doi.org/10.1039/c3ee24441e.
[18] F. Rezaei, A. Mosca, P. Webley, J. Hedlund, P. Xiao, Comparison of traditional and structured adsorbents for CO 2 separation by vacuum-swing adsorption, Ind. Eng. Chem. Res. 49 (2010) 4832–4841, https://doi.org/10.1021/ie9016545.
[19] S. Yun, H. Lee, W.-E. Lee, H.S. Park, Multiscale textured, ultralight graphene monoliths for enhanced CO2 and SO2 adsorption capacity, Fuel 174 (2016) 36–42, https://doi.org/10.1016/j.fuel.2016.01.068.
[20] Y. Han, G. Hwang, H. Kim, B.Z. Haznedaroglu, B. Lee, Amine-impregnated millimeter-sized spherical silica foams with hierarchical mesoporous–macroporous structure for CO2 capture, Chem. Eng. J. 259 (2015) 653–662, https://doi.org/10.1016/j.cej.2014.08.043.
[21] L. Estevez, R. Dua, N. Bhandari, A. Ramanujapuram, P. Wang, E.P. Giannelis, A facile approach for the synthesis of monolithic hierarchical porous carbons – high performance materials for amine based CO2 capture and supercapacitor electrode, Energy Environ. Sci. 6 (2013) 1785, https://doi.org/10.1039/c3ee40549d.
[22] D.P. Vargas, L. Giraldo, J.C. Moreno-Piraján, CO2 adsorption on activated carbon honeycomb-monoliths: a comparison of Langmuir and tóth models, Int. J. Mol. Sci. 13 (2012) 8388–8397, https://doi.org/10.3390/ijms13078388.
[23] S.D. Kenarsari, D. Yang, G. Jiang, S. Zhang, J. Wang, A.G. Russell, Q. Wei, M. Fan, Review of recent advances in carbon dioxide separation and capture, RSC Adv. 3 (2013) 22739, https://doi.org/10.1039/c3ra43965h.

[24] H. An, B. Feng, S. Su, Effect of monolithic structure on CO2 adsorption performance of activated carbon fiber–phenolic resin composite: a simulation study, Fuel 103 (2013) 80–86, https://doi.org/10.1016/j.fuel.2011.06.076.

[25] D.P.V. S, L. Giraldo, J.C. Moreno-Piraján, CO2 adsorption on granular and monolith carbonaceous materials, J. Anal. Appl. Pyrolysis 96 (2012) 146–152, https://doi.org/10.1016/j.jaap.2012.03.016.

[26] M. Nandi, K. Okada, A. Dutta, A. Bhaumik, J. Maruyama, D. Derks, H. Uyama, Unprecedented CO2 uptake over highly porous N-doped activated carbon monoliths prepared by physical activation, Chem. Commun. 48 (2012) 10283, https://doi.org/10.1039/c2cc35334b.

[27] X. Ma, Y. Li, M. Cao, C. Hu, A novel activating strategy to achieve highly porous carbon monoliths for CO 2 capture, J. Mater. Chem. A. 2 (2014) 4819–4826, https://doi.org/10.1039/C3TA14684G.

[28] R.P.P.L. Ribeiro, C.A. Grande, A.E. Rodrigues, Activated carbon honeycomb monolith – zeolite 13X hybrid system to capture CO2 from flue gases employing Electric Swing Adsorption, Chem. Eng. Sci. 104 (2013) 304–318, https://doi.org/10.1016/j.ces.2013.09.011.

[29] L.K.C. de Souza, N.P. Wickramaratne, A.S. Ello, M.J.F. Costa, C.E.F. da Costa, M. Jaroniec, Enhancement of CO2 adsorption on phenolic resin-based mesoporous carbons by KOH activation, Carbon N. Y. 65 (2013) 334–340, https://doi.org/10.1016/j.carbon.2013.08.034.

[30] D. Adinata, W. Wandaud, M. Aroua, Preparation and characterization of activated carbon from palm shell by chemical activation with K2CO3, Bioresour. Technol. 98 (2007) 145–149, https://doi.org/10.1016/j.biortech.2005.11.006.

[31] N. Byamba-Ochir, W.G. Shim, M.S. Balathanigaimani, H. Moon, Highly porous activated carbons prepared from carbon rich Mongolian anthracite by direct NaOH activation, Appl. Surf. Sci. 379 (2016) 331–337, https://doi.org/10.1016/j.apsusc.2016.04.082.

[32] E.L.K. Mui, W.H. Cheung, M. Valix, G. McKay, Activated carbons from bamboo scaffolding using acid activation, Sep. Purif. Technol. 74 (2010) 213–218, https://doi.org/10.1016/j.seppur.2010.06.007.

[33] M. Olivares-Marín, C. Fernández-González, A. Macías-García, V. Gómez-Serrano, Preparation of activated carbon from cherry stones by chemical activation with ZnCl2, Appl. Surf. Sci. 252 (2006) 5967–5971, https://doi.org/10.1016/j.apsusc.2005.11.008.

[34] H. Laksaci, A. Khelifi, M. Trari, A. Addoun, Synthesis and characterization of microporous activated carbon from coffee grounds using potassium hydroxides, J. Clean. Prod. 147 (2017) 254–262, https://doi.org/10.1016/j.jclepro.2017.01.102.

[35] P. González-García, Activated carbon from lignocellulosics precursors: a review of the synthesis methods, characterization techniques and applications, Renew. Sustain. Energy Rev. 82 (2018) 1393–1414, https://doi.org/10.1016/j.rser.2017.04.117.

[36] R. Kumar Jha, H. Bhunia, S. Basu, UV activated monolithic graphene Oxide-Based adsorbents for dynamic CO2 Capture: kinetic, isotherm and thermodynamic studies, Chem. Eng. Sci. 285 (2024) 119572, https://doi.org/10.1016/j.ces.2023.119572.

[37] W.S. Hummers, R.E. Offeman, Preparation of graphitic oxide, J. Am. Chem. Soc. 80 (1958), https://doi.org/10.1021/ja01539a017, 1339–1339.

[38] N. Politakos, I. Barbarin, L.S. Cantador, J.A. Cecilia, E. Mehravar, R. Tomovska, Graphene-based monolithic nanostructures for CO 2 capture, Ind. Eng. Chem. Res. 59 (2020) 8612–8621, https://doi.org/10.1021/acs.iecr.9b06998.

[39] S. Chowdhury, R. Balasubramanian, Holey graphene frameworks for highly selective post-combustion carbon capture, Sci. Rep. 6 (2016) 21537, https://doi.org/10.1038/srep21537.

[40] C. Ma, J. Bai, M. Demir, X. Hu, S. Liu, L. Wang, Water chestnut shell-derived N/S-doped porous carbons and their applications in CO2 adsorption and supercapacitor, Fuel 326 (2022) 125119, https://doi.org/10.1016/j.fuel.2022.125119.

[41] Q. Yu, J. Bai, J. Huang, M. Demir, A.A. Farghaly, P. Aghamohammadi, X. Hu, L. Wang, One-Pot synthesis of melamine formaldehyde resin-derived N-doped porous carbon for CO2 capture application, Molecules 28 (2023) 1772, https://doi.org/10.3390/molecules28041772.

[42] J. Bai, J. Huang, Q. Yu, M. Demir, F.H. Gecit, B.N. Altay, L. Wang, X. Hu, One-pot synthesis of self S-doped porous carbon for efficient CO2 adsorption, Fuel Process. Technol. 244 (2023) 107700, https://doi.org/10.1016/j.fuproc.2023.107700.

[43] J. Zhang, H. Yang, G. Shen, P. Cheng, J. Zhang, S. Guo, Reduction of graphene oxide via <scp>l</scp> -ascorbic acid, Chem. Commun. 46 (2010) 1112–1114, https://doi.org/10.1039/B917705A.

[44] T. Nakajima, A. Mabuchi, R. Hagiwara, A new structure model of graphite oxide, Carbon N. Y. 26 (1988) 357–361, https://doi.org/10.1016/0008-6223(88)90227-8.

[45] R.K. Jha, H. Bhunia, S. Basu, Enhancing CO2 capture through innovating monolithic graphene oxide frameworks, Environ. Res. 249 (2024) 118426, https://doi.org/10.1016/j.envres.2024.118426.

[46] A. Subrati, S. Mondal, M. Ali, A. Alhindi, R. Ghazi, A. Abdala, D. Reinalda, S. Alhassan, Developing hydrophobic graphene foam for oil spill cleanup, Ind. Eng. Chem. Res. 56 (2017) 6945–6951, https://doi.org/10.1021/acs.iecr.7b00716.

[47] J.S. Cho, W. Jang, S.C. Mun, M. Yi, J.H. Park, D.H. Wang, Tuning surface chemistry and morphology of graphene oxide by γ-ray irradiation for improved performance of perovskite photovoltaics, Carbon N. Y. 139 (2018) 564–571, https://doi.org/10.1016/j.carbon.2018.07.010.

[48] S. Verma, R.K. Dutta, A facile method of synthesizing ammonia modified graphene oxide for efficient removal of uranyl ions from aqueous medium, RSC Adv. 5 (2015) 77192–77203, https://doi.org/10.1039/C5RA10555B.

[49] J. Pokhrel, N. Bhoria, S. Anastasiou, T. Tsoufis, D. Gournis, G. Romanos, G.N. Karanikolos, CO2 adsorption behavior of amine-functionalized ZIF-8, graphene oxide, and ZIF-8/graphene oxide composites under dry and wet conditions, Microporous Mesoporous Mater. 267 (2018) 53–67, https://doi.org/10.1016/j.micromeso.2018.03.012.

[50] P. Bhawal, S. Ganguly, T.K. Chaki, N.C. Das, Synthesis and characterization of graphene oxide filled ethylene methyl acrylate hybrid nanocomposites, RSC Adv. 6 (2016) 20781–20790, https://doi.org/10.1039/C5RA24914G.

[51] S. Pei, H.M. Cheng, The reduction of graphene oxide, Carbon N. Y. 50 (2012) 3210–3228, https://doi.org/10.1016/j.carbon.2011.11.010.

[52] L. Stobinski, B. Lesiak, A. Malolepszy, M. Mazurkiewicz, B. Mierzwa, J. Zemek, P. Jiricek, I. Bieloshapka, Graphene oxide and reduced graphene oxide studied by the XRD, TEM and electron spectroscopy methods, J. Electron. Spectrosc. Relat. Phenom. 195 (2014) 145–154, https://doi.org/10.1016/j.elspec.2014.07.003.

[53] E.S. Ganya, N. Soin, S.J. Moloi, J.A. McLaughlin, W.F. Pong, S.C. Ray, Polyacrylate grafted graphene oxide nanocomposites for biomedical applications, J. Appl. Phys. 127 (2020) 054302, https://doi.org/10.1063/1.5135572.

[54] B. Gupta, N. Kumar, K. Panda, V. Kanan, S. Joshi, I. Visoly-Fisher, Role of oxygen functional groups in reduced graphene oxide for lubrication, Sci. Rep. 7 (2017) 45030, https://doi.org/10.1038/srep45030.

[55] D. Tiwari, C. Goel, H. Bhunia, P.K. Bajpai, Melamine-formaldehyde derived porous carbons for adsorption of CO2 capture, J. Environ. Manag. 197 (2017) 415–427, https://doi.org/10.1016/j.jenvman.2017.04.013.

[56] J. Shi, N. Yan, H. Cui, Y. Liu, Y. Weng, D. Li, X. Ji, Nitrogen doped hierarchically porous carbon derived from glucosamine hydrochloride for CO2 adsorption, J. CO2 Util. 21 (2017) 444–449, https://doi.org/10.1016/j.jcou.2017.08.010.

[57] L. Ren, K.N. Hui, K.S. Hui, Y. Liu, X. Qi, J. Zhong, Y. Du, J. Yang, 3D hierarchical porous graphene aerogel with tunable meso-pores on graphene nanosheets for high-performance energy storage, Sci. Rep. 5 (2015) 14229, https://doi.org/10.1038/srep14229.

[58] Y. Xu, K. Sheng, C. Li, G. Shi, Self-assembled graphene hydrogel via a one-step hydrothermal process, ACS Nano 4 (2010) 4324–4330, https://doi.org/10.1021/nn101187z.

[59] Y. Yuan, T.R. Lee, Contact Angle and Wetting Properties, Springer Ser. Surf. Sci., 2013, pp. 3–34, https://doi.org/10.1007/978-3-642-34243-1_1.

[60] W. Ouyang, D. Zeng, X. Yu, F. Xie, W. Zhang, J. Chen, J. Yan, F. Xie, L. Wang, H. Meng, D. Yuan, Exploring the active sites of nitrogen-doped graphene as catalysts for the oxygen reduction reaction, Int. J. Hydrogen Energy 39 (2014) 15996–16005, https://doi.org/10.1016/j.ijhydene.2014.01.045.

[61] S. Chowdhury, R. Balasubramanian, Recent advances in the use of graphene-family nanoadsorbents for removal of toxic pollutants from wastewater, Adv. Colloid Interface Sci. 204 (2014) 35–56, https://doi.org/10.1016/j.cis.2013.12.005.

[62] X. Zhang, Z. Sui, B. Xu, S. Yue, Y. Luo, W. Zhan, B. Liu, Mechanically strong and highly conductive graphene aerogel and its use as electrodes for electrochemical power sources, J. Mater. Chem. 21 (2011) 6494, https://doi.org/10.1039/c1jm10239g.

[63] Z. Xu, Z. Li, C.M.B. Holt, X. Tan, H. Wang, B.S. Amirkhiz, T. Stephenson, D. Mitlin, Electrochemical supercapacitor electrodes from sponge-like graphene nanoarchitectures with ultrahigh power density, J. Phys. Chem. Lett. 3 (2012) 2928–2933, https://doi.org/10.1021/jz301207g.

[64] L.-Y. Meng, S.-J. Park, Effect of exfoliation temperature on carbon dioxide capture of graphene nanoplates, J. Colloid Interface Sci. 386 (2012) 285–290, https://doi.org/10.1016/j.jcis.2012.07.025.
[65] L. Zhou, J. Fan, G. Cui, X. Shang, Q. Tang, J. Wang, M. Fan, Highly efficient and reversible CO 2 adsorption by amine-grafted platelet SBA-15 with expanded pore diameters and short mesochannels, Green Chem. 16 (2014) 4009–4016, https://doi.org/10.1039/C4GC00832D.
[66] V. Presser, J. McDonough, S.-H. Yeon, Y. Gogotsi, Effect of pore size on carbon dioxide sorption by carbide derived carbon, Energy Environ. Sci. 4 (2011) 3059, https://doi.org/10.1039/c1ee01176f.
[67] P.M. Sudeep, T.N. Narayanan, A. Ganesan, M.M. Shaijumon, H. Yang, S. Ozden, P.K. Patra, M. Pasquali, R. Vajtai, S. Ganguli, A.K. Roy, M.R. Anantharaman, P. M. Ajayan, Covalently interconnected three-dimensional graphene oxide solids, ACS Nano 7 (2013) 7034–7040, https://doi.org/10.1021/nn402272u.
[68] Y. Wang, C. Guan, K. Wang, C.X. Guo, C.M. Li, Nitrogen, hydrogen, carbon dioxide, and water vapor sorption properties of three-dimensional graphene, J. Chem. Eng. Data 56 (2011) 642–645, https://doi.org/10.1021/je100840n.
[69] K. Xia, X. Tian, S. Fei, K. You, Hierarchical porous graphene-based carbons prepared by carbon dioxide activation and their gas adsorption properties, Int. J. Hydrogen Energy 39 (2014) 11047–11054, https://doi.org/10.1016/j.ijhydene.2014.05.059.
[70] J. Singh, S. Basu, H. Bhunia, Dynamic CO2 adsorption on activated carbon adsorbents synthesized from polyacrylonitrile (PAN): kinetic and isotherm studies, Microporous Mesoporous Mater. 280 (2019) 357–366, https://doi.org/10.1016/j.micromeso.2019.02.031.
[71] S. Hosseini, E. Marahel, I. Bayesti, A. Abbasi, L. Chuah Abdullah, T.S.Y. Choong, CO2 adsorption on modified carbon coated monolith: effect of surface modification by using alkaline solutions, Appl. Surf. Sci. 324 (2015) 569–575, https://doi.org/10.1016/j.apsusc.2014.10.054.
[72] A.I. Pruna, A. Barjola, A.C. Cárcel, B. Alonso, E. Giménez, Effect of varying amine functionalities on CO2 capture of carboxylated graphene oxide-based cryogels, Nanomaterials 10 (2020) 1446, https://doi.org/10.3390/nano10081446.
[73] T.C. Drage, A. Arenillas, K.M. Smith, C. Pevida, S. Piippo, C.E. Snape, Preparation of carbon dioxide adsorbents from the chemical activation of urea–formaldehyde and melamine–formaldehyde resins, Fuel 86 (2007) 22–31, https://doi.org/10.1016/j.fuel.2006.07.003.
[74] A. Busch, Y. Gensterblum, B.M. Krooss, Methane and CO2 sorption and desorption measurements on dry Argonne premium coals: pure components and mixtures, Int. J. Coal Geol. 55 (2003) 205–224, https://doi.org/10.1016/S0166-5162(03)00113-7.
[75] J. Bai, J. Huang, Q. Yu, M. Demir, E. Akgul, B.N. Altay, X. Hu, L. Wang, Fabrication of coconut shell-derived porous carbons for CO2 adsorption application, Front. Chem. Sci. Eng. (2023), https://doi.org/10.1007/s11705-022-2292-6.
[76] P.M. Sudeep, T.N. Narayanan, A. Ganesan, M.M. Shaijumon, H. Yang, S. Ozden, P.K. Patra, M. Pasquali, R. Vajtai, S. Ganguli, A.K. Roy, M.R. Anantharaman, P. M. Ajayan, Covalently interconnected three-dimensional graphene oxide solids, ACS Nano 7 (2013) 7034–7040, https://doi.org/10.1021/nn402272u.
[77] C. Goel, H. Bhunia, P.K. Bajpai, Synthesis of nitrogen doped mesoporous carbons for carbon dioxide capture, RSC Adv. 5 (2015) 46568–46582, https://doi.org/10.1039/C5RA05684E.
[78] L. Aljerf, High-efficiency extraction of bromocresol purple dye and heavy metals as chromium from industrial effluent by adsorption onto a modified surface of zeolite: kinetics and equilibrium study, J. Environ. Manag. 225 (2018) 120–132, https://doi.org/10.1016/j.jenvman.2018.07.048.
[79] V. Chabot, D. Higgins, A. Yu, X. Xiao, Z. Chen, J. Zhang, A review of graphene and graphene oxide sponge: material synthesis and applications to energy and the environment, Energy Environ. Sci. 7 (2014) 1564, https://doi.org/10.1039/c3ee43385d.
[80] C. Goel, H. Kaur, H. Bhunia, P.K. Bajpai, Carbon dioxide adsorption on nitrogen enriched carbon adsorbents: experimental, kinetics, isothermal and thermodynamic studies, J. CO2 Util. 16 (2016) 50–63, https://doi.org/10.1016/j.jcou.2016.06.002.
[81] O. Hamdaoui, E. Naffrechoux, Modeling of adsorption isotherms of phenol and chlorophenols onto granular activated carbon. Part I. Two-parameter models and equations allowing determination of thermodynamic parameters, J. Hazard Mater. 147 (2007) 381–394, https://doi.org/10.1016/j.jhazmat.2007.01.021.
[82] Y. Liu, J. Wilcox, Effects of surface heterogeneity on the adsorption of CO 2 in microporous carbons, Environ. Sci. Technol. 46 (2012) 1940–1947, https://doi.org/10.1021/es204071g.
[83] V. Krungleviciute, A.D. Migone, M. Yudasaka, S. Iijima, CO 2 adsorption on dahlia-like carbon nanohorns: isosteric heat and surface area measurements, J. Phys. Chem. C 116 (2012) 306–310, https://doi.org/10.1021/jp208766u.
[84] S. Chowdhury, R. Balasubramanian, Highly efficient, rapid and selective CO2 capture by thermally treated graphene nanosheets, J. CO2 Util. 13 (2016) 50–60, https://doi.org/10.1016/j.jcou.2015.12.001.
[85] S.-C. Hsu, C. Lu, F. Su, W. Zeng, W. Chen, Thermodynamics and regeneration studies of CO2 adsorption on multiwalled carbon nanotubes, Chem. Eng. Sci. 65 (2010) 1354–1361, https://doi.org/10.1016/j.ces.2009.10.005.